



Comparative Mid-infrared Spectroscopy of Dark, Primitive Asteroids: Does Shared Taxonomic Class Indicate Shared Silicate Composition?

Oriel A. Humes^{1,2} , Audrey C. Martin³ , Cristina A. Thomas¹ , and Joshua P. Emery¹

¹Northern Arizona University, Flagstaff, AZ 86011, USA; oriel.humes@tu-braunschweig.de

²Technische Universität Braunschweig, Braunschweig, NI 38106, Germany

³University of Central Florida, Orlando, FL 32816, USA

Received 2023 March 9; revised 2024 April 2; accepted 2024 April 2; published 2024 May 6

Abstract

Primitive asteroids with low albedos and red slopes in the visible and near-infrared (VNIR) are found in both the main belt and the Jupiter Trojan clouds. In order to determine whether the VNIR spectral similarities of primitive main-belt asteroids and Jupiter Trojans are reflective of a true compositional similarity, we compare the mid-infrared silicate emission features of main-belt and Jupiter Trojan asteroids. Using archival data from the Spitzer Space Telescope's Infrared Spectrograph and observations from the Stratospheric Observatory for Infrared Astronomy's FORCAST instrument, we analyze the 5–40 μm spectra of 13 primitive main-belt asteroids and compare them to those of Jupiter Trojans in the literature. We find that while many primitive asteroids in the main belt resemble their Trojan counterparts with strong spectral signatures of olivine-rich high-porosity silicate regoliths, we identify (368) Haidea as a spectrally distinctive asteroid that lacks strong evidence of olivine in its mid-IR spectrum. Differences in silicate compositions among D-type asteroids imply a diversity of origins for primitive asteroids.

Unified Astronomy Thesaurus concepts: Asteroids (72); Infrared astronomy (786); Silicate grains (1456); Small Solar System bodies (1469)

1. Introduction

Small solar system bodies, including asteroids and comets, are understood as tracers of the evolutionary history of the solar system. Primitive asteroids—those that have undergone little to no geothermal evolution since their formation—in particular are valuable sources of information about conditions in the early solar system, as their compositions closely reflect the composition of the solar nebula in which they formed. The present-day compositional distribution of asteroids is thought to reflect a combination of initial conditions in the protosolar nebula and the subsequent transport of small bodies (DeMeo & Carry 2013). In general, for large (>50 km) asteroids, the abundance of high-melting-point materials at low heliocentric distances and abundance of relatively more volatile materials at high heliocentric distances suggests that these compositions reflect thermal and chemical gradients within the early solar system (Gradie & Tedesco 1982; DeMeo & Carry 2013). For instance, the presence of hydrated silicates in carbonaceous chondrites, analogs for C-type asteroids common in the main belt, suggests a formation region beyond the water frost line but not so far from the Sun that long orbital timescales preclude the accretion of asteroids prior to the decay of short-lived radionuclides that provide the heat source necessary for thermal alteration to occur (Grimm & McSween 1989). Thus, the locations of primitive C-type asteroids can indicate the availability of water within the solar nebula (e.g., Ceres in McCord & Sotin 2005). On the other hand, the diversity of all asteroid types at small scales throughout the main belt (DeMeo & Carry 2013; DeMeo et al. 2014) provides evidence for substantial migration and mixing among small bodies after

their formation. Both initial compositional gradients and subsequent mixing of asteroid materials are necessary to explain the distribution of asteroids we see today.

The D- and P-type asteroids, characterized by their low albedos and red-sloped, featureless spectra (Tholen 1984; Tholen & Barucci 1989; DeMeo et al. 2009) in the visible and near-infrared (VNIR), are a particularly intriguing population of primitive asteroids (Vilas & Smith 1985). Dynamical modeling has led to the suggestion that Trojan (Morbidelli et al. 2005) and main-belt (Levison et al. 2009) D- and P-types originated from the relatively cooler outer regions of the protoplanetary disk. Their increasing frequency at larger heliocentric distances (Tholen & Barucci 1989; DeMeo & Carry 2013) and spectral resemblance to some outer solar system populations including Centaurs and trans-Neptunian objects (Sheppard 2010) supports this idea. As primitive asteroids, the D- and P-types are thought to have undergone little to no internal differentiation and hydrothermal alteration, thus preserving much of their original compositions (Jones et al. 1990). If the D- and P-types preserve their original compositions, understanding their compositions and distribution may provide unique insights into chemical and dynamical conditions in the early solar system. Previous spectral modeling studies of D- and P-types in the VNIR (Emery & Brown 2004; Sharkey et al. 2019; Gartelle et al. 2021) have proposed compositions rich in silicates with trace amounts of organics and ices, suggestive of an outer solar system origin. However, the lack of VNIR spectral features limits our ability to infer the compositions of these asteroids. Understanding the origin of primitive asteroids is a priority for a number of recent and upcoming spacecraft missions, including the Lucy (Levison et al. 2021) mission.

The Jupiter Trojan population is a major reservoir for D- and P-type asteroids, which comprise the majority of asteroids in the Jovian Trojan swarms (Emery et al. 2010; DeMeo & Carry 2013). The Jupiter Trojans orbit in proximity to the



Original content from this work may be used under the terms of the [Creative Commons Attribution 4.0 licence](https://creativecommons.org/licenses/by/4.0/). Any further distribution of this work must maintain attribution to the author(s) and the title of the work, journal citation and DOI.

Table 1
Physical and Orbital Properties of Primitive Asteroids Examined in This Paper

Asteroid	Semimajor Axis (au)	Eccentricity	Inclination (deg)	H (mag)	Taxonomic Classification
46 Hestia	2.52	0.17	2.35	8.59	P/Xc
65 Cybele	3.44	0.12	3.56	6.89	P/Xc
87 Sylvia	3.48	0.09	10.9	6.98	P/X
140 Siwa	2.73	0.21	3.19	8.5	P/Xc
190 Ismene	3.99	0.17	6.18	7.7	P/X
267 Tirza	2.78	0.10	6.01	10.3	DU/D
269 Justitia	2.62	0.21	5.48	9.79	Ld/IR-RR
336 Lacadiera	2.25	0.10	5.65	9.86	D/Xk
368 Haidea	3.07	0.20	7.8	10	D/
944 Hidalgo	5.73	0.66	42.6	10.56	D/
1268 Libya	3.98	0.10	4.43	9.12	P/
1702 Kalahari	2.86	0.14	9.96	11.1	D/L
3552 Don Quixote	4.26	0.71	31.1	13.07	D/D

Note. Taxonomic classifications are given as (Tholen/SMASSII) classifications from Neese (2017), except in the cases of Justitia, which has been classified using Tholen and the TNO classification scheme from Hasegawa et al. (2021), and Don Quixote, which uses the Tholen/SMASSII classification and comes from Binzel et al. (2004). Note that the IR-RR classification for Justitia indicates that it is redder than the typical D-type.

Sun–Jupiter L4 and L5 Lagrange points, and because of their unique orbital relationship to Jupiter, many dynamical hypotheses have been proposed to explain their emplacement within the Lagrange regions (e.g., Morbidelli et al. 2005; Nesvorný et al. 2013; Pirani et al. 2019). These models demonstrate that the properties of the Trojans we observe today depend both on where the Trojans initially formed and on the subsequent migration history of the giant planets that led to their emplacement within Jupiter’s Lagrange regions. For instance, the Nice model (Morbidelli et al. 2005) predicts a primarily outer solar system origin for Trojans, while the jumping Jupiter (Nesvorný et al. 2013) model predicts that the Trojans sample multiple regions including both the inner and outer solar system. Probing the relationship between D- and P-types in the main-belt and Trojan swarms can provide an observational test for these models of giant planet migration. For example, the Nice model predicts a common, specifically outer solar system parent population for D- and P-types across the main-belt, Hilda, and Trojan populations (Levison et al. 2009).

In contrast to the relatively featureless VNIR, in the mid-infrared, many D- and P-type asteroids exhibit 10 and 20 μm silicate emission features (Emery et al. 2006; Mueller et al. 2010; Licandro et al. 2011). These features are diagnostic of both physical and chemical properties of silicates, including regolith porosity (Martin et al. 2022, 2023), Mg# (the ratio of magnesium to iron in a mineral lattice) for both pyroxenes (Hamilton 2000; Chihara et al. 2002) and olivines (Koike et al. 2003; Hamilton 2010; Lane et al. 2011), amorphous versus crystalline mineral structure (Martin & Emery 2023), and a silicate hydration state (Beck et al. 2014; McAdam et al. 2015). The compositional properties as revealed by silicate emission features in the mid-infrared ($\sim 5\text{--}40\ \mu\text{m}$) are indicative of the formation region, as temperature conditions within the initial solar nebula influence the materials and formation pathways available to condense silicates at varying heliocentric distances (Gail 2004; Henning 2010; Morlok et al. 2014). In Martin & Emery (2023), the silicate emissivity spectrum was characterized in detail to determine the composition and regolith porosity of several Jupiter Trojans. That study concluded that

Jupiter Trojans likely originate from the outer solar system due to the abundance of magnesium-rich silicates, absence of hydrated silicates, and high-porosity regoliths similar to those of comets.

In this paper, we examine the spectra of 13 D- and P-type asteroids as observed by the Stratospheric Observatory for Infrared Astronomy (SOFIA) and Spitzer Space Telescope (see Table 1). This group samples objects in the main-belt, Cybele, and near-Earth populations but not the Trojans previously characterized in Martin & Emery (2023). We examine silicate emission features in the mid-infrared to compare the spectra of main-belt D- and P-types and literature spectra of Jupiter Trojan D- and P-types (Emery et al. 2006; Martin & Emery 2023) to determine whether these two populations, which are similar in the VNIR, resemble each other in the mid-infrared. Similarities in silicate compositions among these two populations would point to a shared region of origin for primitive asteroids across the Trojan and main-belt populations, while compositional differences would indicate separate parent populations for primitive main-belt and Trojan asteroids. Determining whether primitive asteroids in the main belt share the outer solar system origin suggested by Martin & Emery (2023) for the Trojans will allow us to determine the extent of mixing between inner and outer solar system materials within the main belt and provide new observational constraints on formation and emplacement mechanisms for primitive asteroids. Constraining the amount of outer solar system material that has been delivered to the main belt and inner solar system subsequently will lead to a greater understanding of the mechanisms responsible for delivering volatiles from beyond the frost line to the inner solar system.

2. Methods

2.1. Spitzer Space Telescope Observations

We identified 11 non-Trojan D- and P-type asteroids in the Spitzer Heritage Archive. These asteroids were observed using the Infrared Spectrograph (IRS) instrument (Houck et al. 2004) by programs IRS_P/666 and IRS_R/668 (IRS Campaigns P and R by PI James R. Houck) and ASTEROIDS-1/88 and

Table 2
Observation Circumstances for D- and P-type Asteroids in the Spitzer Heritage Archive

Asteroid	Modes	Program	Obs. Time (UTC)	Exp. Time (s)	r (au)	Δ (au)	Phase Angle (deg)
65 Cybele	Spitzer SH	ASTEROIDS-2/91	2005-Feb-08 6:05	12	3.79	3.30	14.1
	Spitzer SL	ASTEROIDS-2/91	2005-Feb-08 6:00	43	3.79	3.3	14.1
87 Sylvia	Spitzer SH, LH	ASTEROIDS-1/88	2004-Nov-12 6:40	12, 13	3.22	2.71	17.1
	Spitzer SL	ASTEROIDS-1/88	2004-Nov-12 5:47	26	3.22	2.71	17.1
140 Siwa	Spitzer SL	ASTEROIDS-2/91	2004-Feb-29 9:01	14	2.65	2.23	21.4
267 Tirza	Spitzer SL, LL	ASTEROIDS-2/91	2005-Nov-17 1:40	135, 25	3.02	2.97	19.6
269 Justitia	Spitzer SL	ASTEROIDS-2/91	2005-Apr-15 7:54	25	2.12	1.66	27.5
336 Lacadiera	Spitzer SL	ASTEROIDS-2/91	2004-Oct-03 17:29	24	2.43	1.96	24.0
368 Haidea	Spitzer SL, LL	ASTEROIDS-1/88	2004-Mar-25 23:29	46, 25	3.69	3.15	14.1
944 Hidalgo	Spitzer SL, LL	ASTEROIDS-2/91	2006-Jul-24 10:18	53, 25	1.96	1.71	30.7
1268 Libya	Spitzer SL, LL	IRS_P/666, IRS_R/668	2003-Nov-16 10:32	609, 148	4.19	4.00	13.9
1702 Kalahari	Spitzer SL, LL	ASTEROIDS-2/91	2005-Jul-03 4:42	513, 58	3.09	2.67	18.6
3552 Don Quixote	Spitzer LL	ASTEROIDS-1/88	2004-Mar-23 4:43	4696	6.91	6.49	7.76

Note. For each asteroid, we report the modes used to observe the asteroid, the associated observing program, the mean observation time, the total exposure time for each mode, and the observational geometries including heliocentric distance r , distance from the asteroid to the telescope Δ , and phase angle as calculated by the JPL Horizons online ephemeris.

ASTEROIDS-2/91 (Extinct Comets and Low-Albedo Asteroids and Extinct Comets and Low-Albedo Asteroids 2 by PI Dale Cruikshank). These targets included observations in all four IRS modes: short-low (SL; 5.2–14.5 μm), long-low (LL; 14.0–38.0 μm), short-high (SH; 9.9–19.6 μm), and long-high (LH; 18.7–37.2 μm). Observations in any one of these modes are useful for identifying silicate emission features, as the SL and SH modes cover the 10 μm region and the LL and LH modes cover the 20 μm region, and the choice of observing mode was influenced by the brightness of individual targets. For observations in the low-resolution modes (SL and LL), background pair subtraction was performed by pairing images in two different nod positions. In some cases (e.g., Siwa), the two nod positions resulted in the spectral trace falling on two different regions of the same section of the chip, while most asteroids had spectra that nodded between the two different sections of the chip (i.e., orders 1 and 2 versus order 3). For observations in the high-resolution modes (SH and LH), background subtraction was done by subtracting the average of shadow observations taken of empty sky at the observed location of the asteroid after some time had passed and the asteroid had moved. While SH and LH spectra were available for Siwa and Lacadiera in these modes, the lack of corresponding “shadow” observations prevented these additional spectra from being extracted since they lacked an appropriate measurement of background.

After background subtraction, the spectra were extracted using the Spitzer IRS Custom Extraction software, following the general procedure outlined in Recipe 16 of the Spitzer Data Analysis Cookbook (Spitzer Science User Support and Instrument Teams and IRSA Science User Support Team 2017). Next, the extracted spectra were adjusted so that each order was scaled to the same flux value in regions where the orders overlapped. This was accomplished by fitting low- (first, second, or third) order polynomials to the data, then determining the resulting multiplicative scaling factor necessary such that the polynomials would have the same value—that is, the mean of the predicted fluxes—at a specific wavelength. For some data, obvious outliers due to instrumental effects (e.g., the SL teardrop at long wavelengths) were excluded from the fit to ensure better alignment of the orders.

For the SL and LL observations, the alignment wavelengths were 7.5 and 21 μm , respectively; that is, each spectrum was scaled to the average predicted flux measurement of all orders at 7.5 or 21 μm . For asteroids with both SL and LL observations, we aligned the two modes to the average predicted flux at 15 μm . For the SH and LH observations, no single wavelength region overlaps in all spectral orders, so the predicted fluxes and scale factors required to align the spectral orders were calculated at wavelengths of 10.5, 11, 11.65, 12.4, 13.1, 14.3, 15.1, 16.4, and 17.8 μm for the SH and 20.5, 21, 22.5, 24, 25.5, 27, 29, 31.25, and 34 μm for the LH data, then scaled by the average of all the scale factors calculated for each mode. This has the effect of weighting each region of overlap equally. This scaling process is similar to the one described in Emery et al. (2006).

For most asteroids, only two spectra were taken, but for some especially bright targets (e.g., the SL observations of Cybele, Sylvia, Justitia, Lacadiera, Hidalgo, Libya, Tirza, and Siwa), IRS was used in mapping mode to ensure the target was well centered in the slit. Rather than using the peak-up cameras to locate the centroid of the target, which saturated for bright targets, observations were taken by stepping across the disk of the asteroid to ensure at least one pair of observations was well centered in the slit. In these instances, only the brightest pair of extracted spectra was used in the rest of the analysis to exclude observations that were not well centered in the slit. While LH observations of Cybele and corresponding shadow observations exist in the Spitzer Heritage Archive, the fluxes at the long-wavelength end of the SH data did not match the fluxes at the short-wavelength end of the LH data at 19 μm , indicating that in the LH data, the asteroid was not well centered in the slit. Therefore, we exclude the LH data for Cybele in our analysis. A summary of the Spitzer observations and their observing circumstances can be found in Table 2.

We note that the Spitzer IRS spectra of several asteroids already exist in the published literature. In particular, Spitzer IRS spectra of 65 Cybele (Licandro et al. 2011), 87 Sylvia (Marchis et al. 2012), 386 Haidea (Vernazza et al. 2013), 944 Hidalgo (Lowry et al. 2022), and 3552 Don Quixote (Mommert et al. 2014) have been examined by previous authors. In these cases, we rereduced the data starting from the Level 2 data

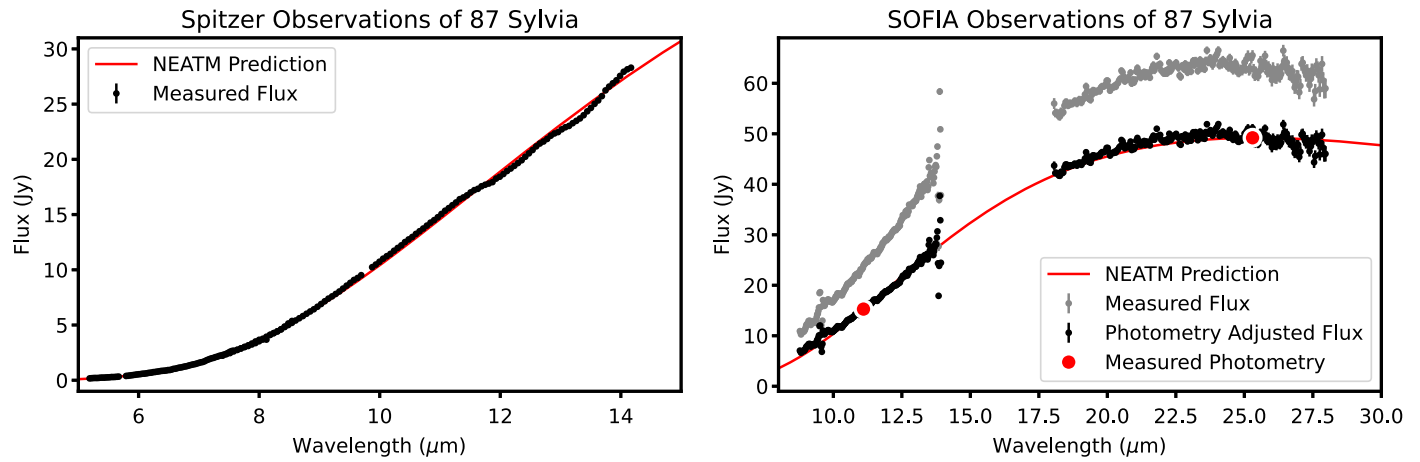


Figure 1. Comparison of the NEATM predictions to the measured fluxes of 87 Sylvia as observed using the Spitzer Space Telescope (left) and SOFIA (right). For SOFIA observations, spectra are scaled using a multiplicative factor to match the photometric measurements of the asteroid obtained on the same flight (see Section 2.2 of the text for details). The analogous scaling procedure for the Spitzer data is described in Section 2.1 of the text, but the unaligned Spitzer data are excluded from the figure, as the difference between the aligned and unaligned fluxes is not visible on the scale of the figure.

Table 3
Observation Circumstances for Primitive Asteroids Using SOFIA

Asteroid	Filters/Grisms	Exposure Times (s)	Obs. Time (UTC)	r (au)	Δ (au)	Phase Angle (deg)
46 Hestia	G227	544	2021-Jun-30 5:32	2.63	1.87	17.5
	G111, G227, F111, F253	838, 454, 46.4, 36.2	2021-Jul-09 5:14	2.62	1.95	19.6
87 Sylvia	G111, G227, F111, F253	1280, 699, 67.1, 55.8	2022-May-24 6:47	3.55	2.58	5.37
140 Siwa	G111, G227, F111, F253	935, 349, 70.3, 53.7	2022-May-27 5:36	2.51	1.61	13.1
190 Ismene	G227, F253	1360, 44.6	2022-Feb-02 8:33	3.41	2.46	5.17
	G111, F111	2350, 70.9	2022-Feb-09 9:14	3.41	2.5	7.23

Note. For each asteroid, we report the filters used to observe the asteroid, the mean observation time, the total exposure time for each filter, and the observational geometries including heliocentric distance r , distance from the asteroid to the telescope Δ , and phase angle as calculated by the JPL Horizons online ephemeris.

products available in the Spitzer Heritage Archive to ensure consistency between all asteroids in our data set in the reduction and thermal modeling process.

2.2. SOFIA Observations

In addition to the Spitzer observations described above, we also observed four primitive asteroids using SOFIA. We observed these asteroids using the Faint Object infraRed Camera for the SOFIA Telescope (FORCAST) instrument (Herter et al. 2018) as part of program 08_0105 (Mid-Infrared Spectroscopy of Primitive Asteroids in the Middle Solar System by PI Oriel Humes). Each asteroid was observed using the G111 and G227 grisms along with contemporaneous imagery in the F111 and F253 filters. Initial processing of these images, including background subtraction and spectral extraction, were performed by the Universities Space Research Association, and the extracted spectra and background-subtracted images were downloaded directly from the Infrared Science Archive. We located the centroid of each asteroid in the F111 and F253 images and then performed background-subtracted aperture photometry using an object radius of 12 pixels and a background annulus with inner and outer radii of 15 and 25 pixels, respectively, according to the procedure described in the FORCAST Basic Photometry cookbook (SOFIA/USRA 2022a). We then used the photometric measurements to align the G111 and G227 spectra for each asteroid. By convolving the object spectra and the transmission spectra of the F111 and F253 filters (SOFIA/USRA 2022b),

we computed the predicted F111 and F253 photometric fluxes. Using the ratio between the predicted and actual fluxes, we calculated the multiplicative factor needed to bring the grism spectra into alignment with the measured photometry such that the predicted convolved fluxes were equal to the measured photometry. While this procedure generally follows the procedure outlined in the FORCAST Grism Spectra: Basic Inspection and Assessment notebook in SOFIA/USRA (2022b), we used a multiplicative (rather than additive) correcting factor to align our spectra to the photometry (see Figure 1, right panel). Our rationale is that in order to convert from flux to emissivity, we must divide by a model of the blackbody emission of the asteroid. An additive correction factor would then distort the shape of the resulting emissivity spectrum, while a multiplicative factor would maintain its shape. Using a multiplicative factor also parallels the process of aligning the spectral orders of the Spitzer data as described above. A summary of the SOFIA observations and their observing circumstances can be found in Table 3.

2.3. Thermal Modeling

Both the Spitzer Space Telescope and SOFIA observe the thermal emission from asteroids in janskys. In order to convert from a thermal emission spectrum to an emissivity spectrum, we must model the predicted thermal emission for each asteroid, then divide the emission data by this predicted emission spectrum to obtain an emissivity spectrum (Harris 1998, see Figure 1). The Near Earth Asteroid Thermal

Model (NEATM), while initially developed to model thermal emission of near-Earth asteroids, is commonly used to predict thermal fluxes for main-belt and Trojan asteroids throughout the literature (e.g., Emery et al. 2006; Licandro et al. 2011; Hargrove et al. 2012). By equating incoming solar energy (a factor of the geometric albedo a) and outgoing thermal emission, this model computes the thermal emission due to solar heating at each point on the sunlit hemisphere of an asteroid (the contribution from the unlit hemisphere is assumed to be 0). Then, using the geometric circumstances of the observation, the flux received by the observer is computed by integrating the predicted emission over the hemisphere visible to the observer (Harris 1998). In addition to the geometric factors, the NEATM we used also includes two empirical corrections: a beaming parameter η to correct for surface roughness and an emissivity-like multiplicative correction factor ϵ that represents the ratio of observed to predicted flux. The variation in these empirical correction factors encapsulates the contributions of observational factors not taken into account by the thermal model, such as variable surface emissivity and slit losses.

For our observations, we used the NEATM included in the `mskpy` surfaces package developed for python by Michael Kelley (2021). This model uses χ^2 minimization to derive the best-fit diameter and beaming parameter η given the observing geometry, albedo, and average emissivity and computes the corresponding modeled fluxes at a given wavelength. We assumed an average emissivity of $\epsilon = 0.9$, the mean emissivity for asteroids as reported in Mainzer et al. (2011). Both the diameter and the beaming parameter are free to vary in the χ^2 minimization routine. To convert from flux to emissivity, we divided the fluxes as measured by the telescope by the modeled flux, then multiplied by the assumed average bolometric emissivity. To derive errors on the diameter and beaming parameter, we assume an additional uncertainty in flux to account for uncertainty in the absolute photometric calibration of the spectra in addition to reported error measurements. For Spitzer, we assume this uncertainty is 10%, following the findings of Decin et al. (2004). For the SOFIA data, the absolute flux is calibrated using photometry, and we take the average uncertainty to be (5.6%), the average error in photometry across all our targets. After computing the NEATM-derived diameter, beaming parameter, and their associated errors, we propagate the expected error due to absolute flux uncertainty by adding the expected uncertainty in quadrature to the NEATM-derived errors. In most cases, the error associated with absolute flux uncertainty dominates the error term. For most asteroids, we used a single NEATM to model the flux; that is to say that both short-wavelength spectra (e.g., from Spitzer SL or SOFIA G111) and long-wavelength spectra (e.g., from Spitzer LL or SOFIA G227) were combined into a single spectrum that was used as input into the thermal model if the observations were taken on the same day. For 368 Haidea and 1702 Kalahari, we found that the long-wavelength end of the Spitzer SL spectrum was heavily affected by the SL teardrop, a noted artifact affecting this region of Spitzer spectra. The artifact led to difficulty in aligning the SL and LL spectra. For these two asteroids, we fit a separate NEATM for the SL and LL segments.

3. Results

3.1. Emissivity Spectra and Thermal Modeling

The results of the NEATM modeling are summarized in Table 4. We note good agreement between the reported literature values and NEATM-derived diameters, with a few exceptions. First, the June SOFIA G227 observations of 46 Hestia do not agree with the literature values for diameter. These observations were taken without contemporaneous photometry, so these spectra could not be scaled to account for potential slit losses. Accordingly, the NEATM-derived diameter and beaming parameter are lower for this observation than for the other observation of 46 Hestia. For this observation in particular, the June SOFIA G227 observations were converted to emissivity by dividing by the thermal model, then multiplying the resulting emissivity spectrum by a scaling factor to align the June G227 observations that lacked photometry to the July G227 observations. These two G227 observations were averaged together to produce the final G227 spectrum of 46 Hestia, so the June values of the beaming parameter and diameter are likely a reflection of observation circumstances (e.g., slit misalignment) rather than reflective of a true physical property of 46 Hestia.

Another exception is 65 Cybele. Using the same Spitzer data set, Licandro et al. (2011) found that 65 Cybele had an estimated diameter of 290 ± 5 km. Our diameter estimate for 65 Cybele is much larger than the NEOWISE diameter but is consistent with the diameter derived by Licandro et al. (2011), suggesting the difference between the derived diameter values is due to observing 65 Cybele at different epochs. Temporal variation, including the temporally varying cross section of a rotating asteroid, or differences in data processing, such as rotational or seasonal averaging of thermal fluxes used to estimate diameter, may account for the differences in reported literature diameter and derived diameter for asteroids like 87 Sylvia and 140 Siwa, whose diameter values differ by many standard deviations. This interpretation is further supported by the Marchis et al. (2012) diameter estimate. That work estimated the diameter of 87 Sylvia in the Spitzer SL data to be 272.4 ± 13.4 km, in agreement with our 263 ± 13 km diameter derived from the same data set. Therefore, variations in Sylvia's derived diameter likely reflect varying observation circumstances between observing epochs. The results of our thermal modeling can be further validated by comparing the derived NEATM parameters from previous spectroscopic observations and independently computed thermophysical models of the same Spitzer archival data. In Mommert et al. (2014), the diameter of 3552 Don Quixote is estimated as 18.4 ± 0.04 km. The diameter estimates for these asteroids are in agreement with the diameter estimates of the thermal model presented in this paper. Vernazza et al. (2013) present an emissivity spectrum of 368 Haidea; that paper does not report an estimated size. Similarly, diameter is not a varied parameter in the thermophysical modeling of 944 Hidalgo in Lowry et al. (2022).

3.2. Feature Characterization

We present the complete SOFIA spectra (8–14 μm and 18–28 μm) in Figure 2. The results of our reduction of the Spitzer Space Telescope spectra (5–40 μm) are shown in Figures 3 and 4. In general, the Spitzer spectra tend to show a sharp emissivity dip at short wavelengths, followed by the

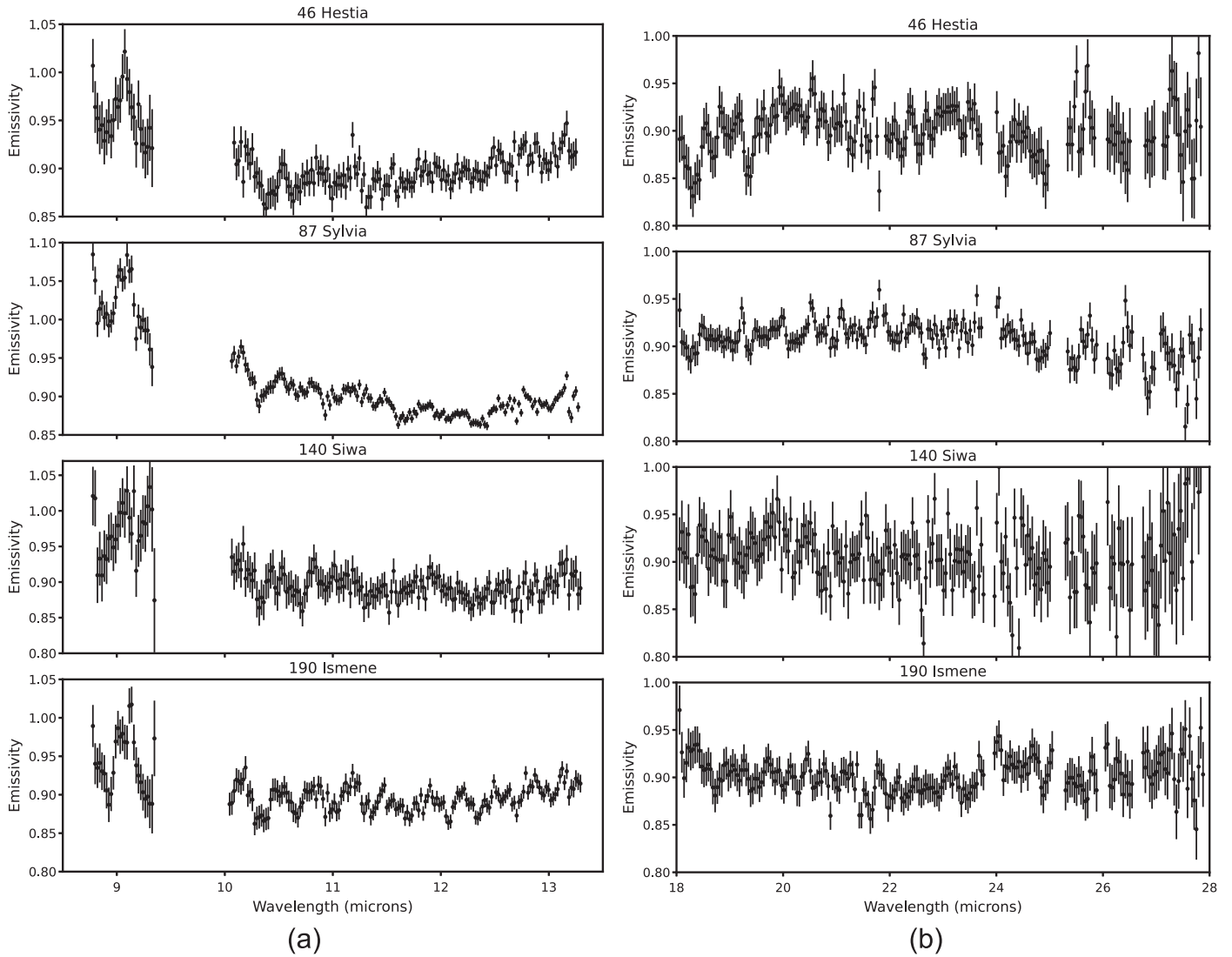


Figure 2. Mid-infrared spectra of asteroids 46 Hestia, 87 Sylvia, 140 Siwa, and 190 Ismene as observed by the SOFIA FORCAST instrument using the G111 (panel (a)) and G227 (panel (b)) grisms. Note that we do not display data points for which atmospheric transparency is low (<0.9).

broad $10\ \mu\text{m}$ silicate feature in emission. At longer wavelengths, the spectra tend to show additional silicate features around 15 and $20\ \mu\text{m}$ followed by a flat or linear continuum. To describe the general shapes of the features, we employ the terminology used in Kelley et al. (2017) to compare the mid-infrared spectra of comets and Jupiter Trojans: the broad $10\ \mu\text{m}$ features are characterized as trapezoidal, rounded, or present.

Among our sample, we see trapezoidal $10\ \mu\text{m}$ features in the Spitzer spectra of 65 Cybele, 87 Sylvia, 267 Tirza, and 944 Hidalgo. These asteroids all show sharp shoulders (e.g., a change in slope from the relatively flat slope of the $10\ \mu\text{m}$ plateau to a decreasing slope) near $11\ \mu\text{m}$, bounding the long-wavelength edge of the emission features.

We see rounded $10\ \mu\text{m}$ features in the spectra of 269 Justitia, 336 Lacadiera, 1268 Libya, and 1702 Kalahari. These asteroids show $10\ \mu\text{m}$ features bounded by dips at 8 and $12\ \mu\text{m}$ like the trapezoidal asteroids, but the shoulder at $11\ \mu\text{m}$ is less distinct but still present. 386 Haidea also has a rounded $10\ \mu\text{m}$ feature, but unlike the previous examples, 386 Haidea lacks a peak or shoulder near $11\ \mu\text{m}$. Instead, the spectrum of 386 Haidea begins to turn downward at $10.55\ \mu\text{m}$.

Without complete coverage of the short-wavelength end of the $10\ \mu\text{m}$ feature, it is harder to classify the shapes of the $10\ \mu\text{m}$ feature in the SOFIA data. The general decrease in emissivity from 10 to $12.5\ \mu\text{m}$ is evidence of the $10\ \mu\text{m}$ silicate emission feature in the SOFIA spectrum of 87 Sylvia. Similarly, the higher average emissivities from 10 to $11\ \mu\text{m}$ and presence of the $12.5\ \mu\text{m}$ dip in the SOFIA spectra of both 87 Sylvia and 140 Siwa (which is associated with and defines the long-wavelength edge of the $10\ \mu\text{m}$ feature) suggest that the $10\ \mu\text{m}$ feature is present in the spectra of both these asteroids. For 190 Ismene, interpretation of spectral features is complicated by the presence of a systematic, high-frequency “wiggle” in wavelength space present in the G111 spectrum (8 – $14\ \mu\text{m}$), which shows a series of regular peaks separated by $\sim 0.34\ \mu\text{m}$ across the short-wavelength portion of the spectrum. The other SOFIA spectra may be similarly affected by high-frequency noise. For 46 Hestia, we see an increase in emissivity from 10 to $12.5\ \mu\text{m}$ and an absence of a clear high-wavelength bound on the $10\ \mu\text{m}$ feature suggesting that the $10\ \mu\text{m}$ feature is not present in emission at all. From 10 to $13\ \mu\text{m}$, the spectrum of 87 Sylvia is consistent (aside from high-frequency noise that

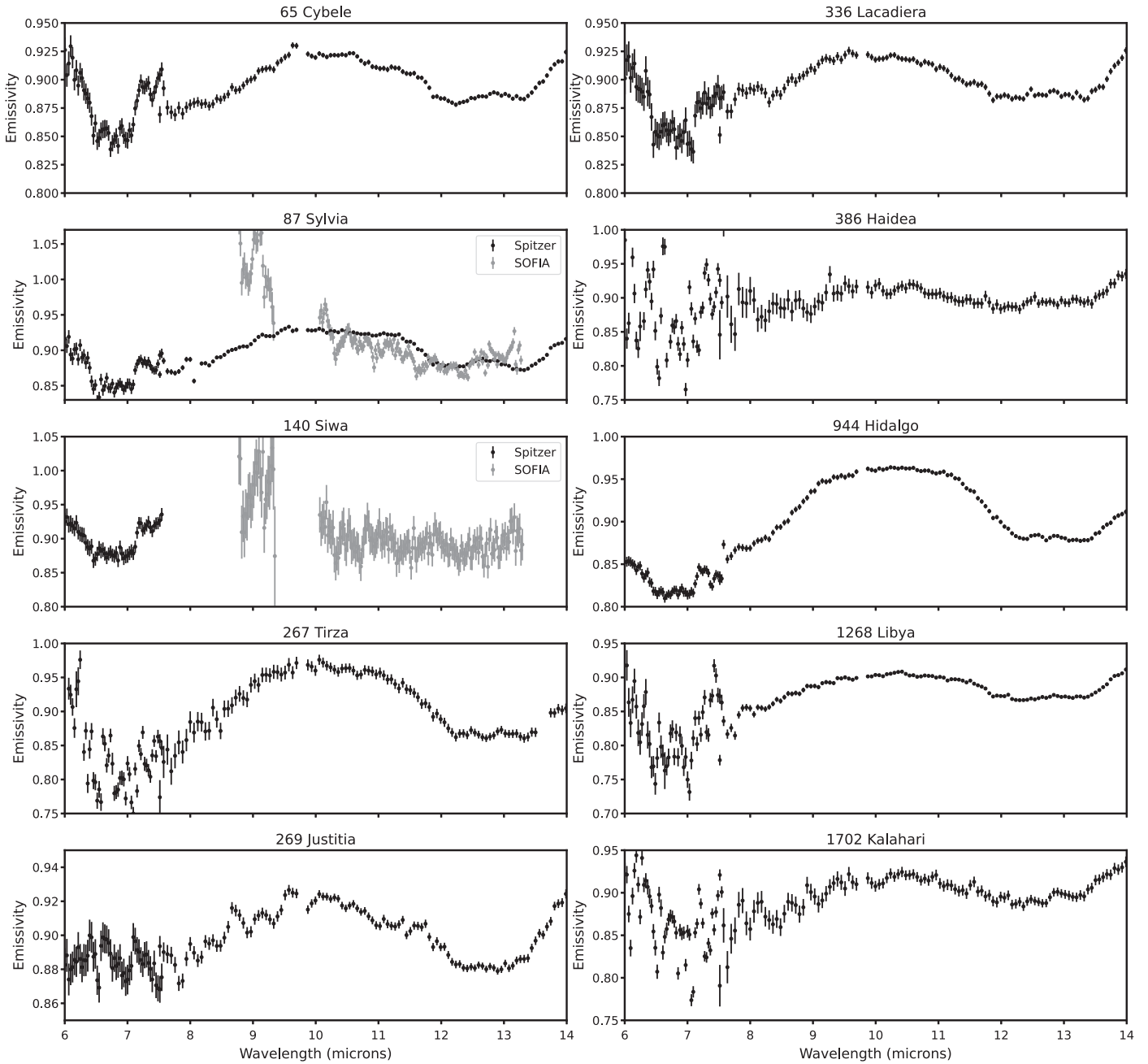


Figure 3. Mid-infrared spectra of asteroids 65 Cybele, 87 Sylvia, 140 Siwa, 267 Tirza, 269 Justitia, 336 Lacadiera, 386 Haidea, 944 Hidalgo, 1268 Libya, and 1702 Kalahari from 6 to 14 μm as observed by the Spitzer IRS instrument in SL mode. For 87 Sylvia and 140 Siwa, we also overplot the SOFIA FORCAST G111 observations scaled to the same average emissivity for comparison. See also Licandro et al. (2011), Marchis et al. (2012), Vernazza et al. (2013), and Lowry et al. (2022) for their analyses of the same Spitzer IRS spectra of 65 Cybele, 87 Sylvia, 386 Haidea, and 944 Hidalgo, respectively.

may be atmospheric) in both the SOFIA and Spitzer data. We note a discrepancy in the Spitzer and SOFIA spectra at the shortest SOFIA wavelengths ($\sim 9 \mu\text{m}$), where the SOFIA spectrum of 87 Sylvia has a much higher emissivity than the Spitzer data. We see similar extremely high emissivities at the shortest wavelengths ($5\text{--}6 \mu\text{m}$) of the Spitzer SL data as well, suggesting that the thermal model struggles to match the data in regions of particularly low flux (e.g., at the shortest wavelengths for any particular instrument). Given the higher signal-to-noise ratio and more complete wavelength coverage, we defer to the Spitzer spectra of 87 Sylvia in our analyses.

To determine the precise locations of spectral features in each asteroid spectrum (See Table 5), we used a Monte Carlo

estimation method. For each asteroid in our sample, we generated 1000 synthetic asteroid spectra by drawing emissivity values from a Gaussian distribution centered around the emissivity value of each data point with a standard deviation equal to the error for that point. Then, for each synthetic spectrum, we fit a fourth-order polynomial spline to smooth the data, resulting in 1000 smoothed splines for each spectrum. Using a polynomial spline allows the local extrema of the spectrum to be efficiently identified, as the derivatives of the polynomials are straightforward to compute. To identify a particular local maximum (minimum), we first identify a range over which to determine the maximum (minimum) visually, then calculate the local extrema for each spline by determining

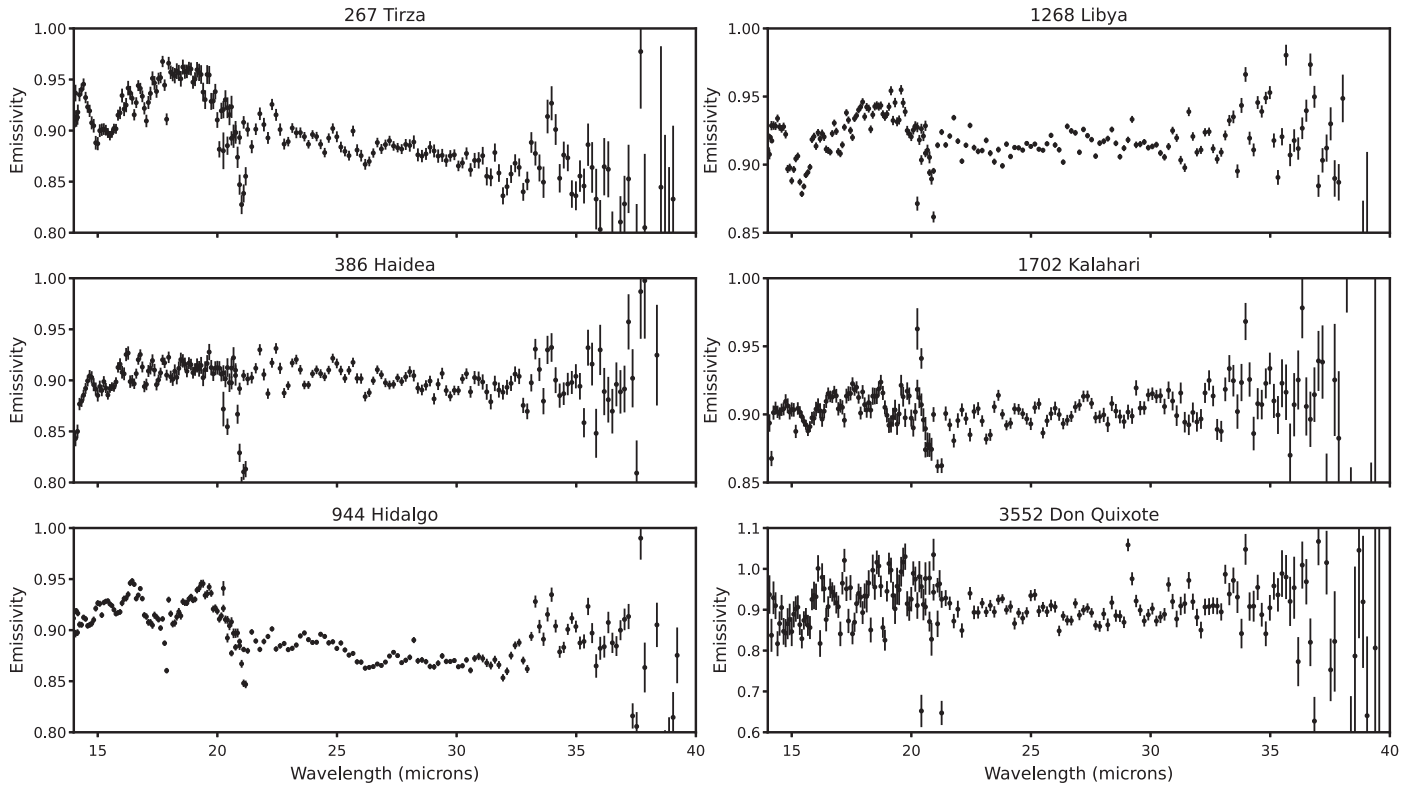


Figure 4. Mid-infrared spectra of asteroids 267 Tirza, 386 Haidea, 944 Hidalgo, 1268 Libya, 1702 Kalahari, and 3552 Don Quixote from 14 to 40 μm as observed by the Spitzer IRS instrument in LL mode. See also Vernazza et al. (2013), Mommert et al. (2014), and Lowry et al. (2022) for their analyses of the same Spitzer IRS spectra of 368 Haidea, 944 Hidalgo, and 3552 Don Quixote, respectively.

where its derivative is 0. In the case where there are multiple points with a derivative of 0, we evaluate the spline at each point and take the wavelength corresponding to the maximum (minimum) value as the location of the local maximum (minimum). Given the locations of the spline maxima (minima) in wavelength space, we then fit a Gaussian to these measurements to get an average feature position (corresponding to the mean) and error (corresponding to the standard deviation) of the distribution of measurements. Repeating this process for different local extrema allows us to measure the position of various features in the spectrum. This procedure is similar to the feature measurement process described in Martin & Emery (2023) and, in further detail, in Martin (2022).

In addition to measuring the locations of various features, we also use the methods described in Martin et al. (2022) and Martin & Emery (2023) to characterize the shape of the 10 μm silicate emission feature to enable direct comparison of the spectral features of our main-belt sample to the Trojans (see Figure 5). In Martin & Emery (2023), local minima near 8 and 12 μm are used to define the bounds of the silicate emission feature. In particular, the minimum at 8 μm is bounded on the lower-wavelength side by a sharp dip in emissivity that identifies the edge of the feature. For two asteroids (368 Haidea and 1702 Kalahari) in our sample, we identify the feature edge closer to 7 than 8 μm because of the location of this sharp dip. Once the bounds are identified using the procedure described previously to locate local extrema, the mean locations of the 8 and 12 μm features are used to define endpoints for a linear continuum, which can be subtracted from the spectrum to isolate the spectrum of the 10 μm feature itself. We parameterize the feature by its width, continuum slope, spectral contrast, and skew (see Table 6) as follows.

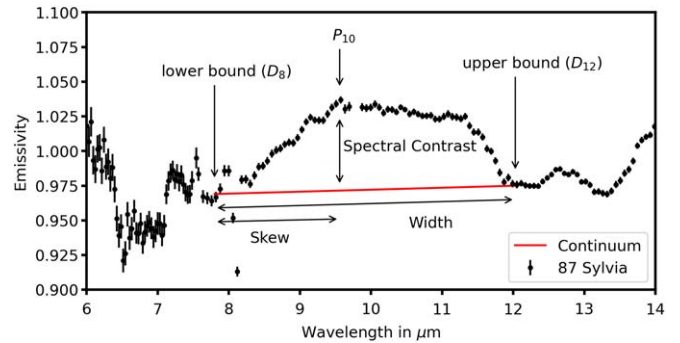


Figure 5. Graphical explanation of the band parameters of the 10 μm feature, with the spectrum of 87 Sylvia, normalized to an average emissivity of 1, as an example. Band parameters are measured as described in Martin (2022), except for skew (see text).

1. Width is measured by subtracting the locations of the 12 and 8 μm bounds.
2. Continuum slope is given by the slope of the linear continuum passing between the 12 and 8 μm bounds.
3. To obtain spectral contrast, we normalize the spectrum to a mean emissivity of 1, then determine the location of the continuum-removed peak near 9.8 μm . Subtracting the emissivity at this peak by the predicted emissivity from the continuum gives a difference in emissivity that can be multiplied by 100 to give a percentage increase in emissivity.
4. We measure skew as a proportion, dividing the distance from the 9.8 μm peak to the 8 μm bound by the width of the feature. A left-skewing feature has a skew of <0.5 , indicating that the continuum-removed peak falls at

Table 4
Results of Thermal Modeling

Asteroid	Instrument/Mode	Literature Diameter (km)	Literature Albedo	Derived Diameter (km)	Derived Beaming Parameter
46 Hestia	SOFIA G227	131 ± 22‡	0.046 ± 0.015‡	90.5 ± 3.0*	0.47 ± 0.03*
	SOFIA G111 and G227	131 ± 22‡	0.046 ± 0.015‡	132 ± 3.7	0.96 ± 0.01
65 Cybele	Spitzer SH	237 ± 4.2†	0.071 ± 0.003†	289 ± 15	0.97 ± 0.02
	Spitzer SL	237 ± 4.2†	0.071 ± 0.003†	292 ± 15	0.94 ± 0.01
87 Sylvia	Spitzer SH and LH	253 ± 3.0‡	0.046 ± 0.004‡	246 ± 12	0.96 ± 0.01
	Spitzer SL	253 ± 3.0‡	0.046 ± 0.004‡	263 ± 13	0.98 ± 0.01
	SOFIA G111 and G227	253 ± 3.0‡	0.046 ± 0.004‡	267 ± 7.3	0.89 ± 0.01
140 Siwa	Spitzer SL	110 ± 3.0†	0.068 ± 0.004†	92.6 ± 4.7	0.87 ± 0.01
	SOFIA G111 and G227	110 ± 3.0†	0.068 ± 0.004†	98.4 ± 2.7	0.76 ± 0.01
190 Ismene	SOFIA G227	159	0.066	180 ± 5.3	0.84 ± 0.02
	SOFIA G111	159	0.066	174 ± 5.2	0.75 ± 0.01
267 Tirza	Spitzer SL and LL	56.0 ± 0.6‡	0.051 ± 0.008‡	55.1 ± 2.7	0.91 ± 0.01
269 Justitia	Spitzer SL	50.7 ± 0.2‡	0.061 ± 0.007‡	50.5 ± 2.5	0.84 ± 0.01
336 Lacadiera	Spitzer SL	63.4 ± 11‡	0.054 ± 0.023‡	69.9 ± 3.5	0.99 ± 0.01
368 Haidea	Spitzer SL	69.3 ± 0.2‡	0.038 ± 0.007‡	66.7 ± 3.3	0.88 ± 0.01
	Spitzer LL	69.3 ± 0.2‡	0.038 ± 0.007‡	67.1 ± 3.4	0.84 ± 0.01
944 Hidalgo	Spitzer SL and LL	38.0	0.060	45.6 ± 2.3	0.77 ± 0.01
1268 Libya	Spitzer SL	96.7 ± 1.2‡	0.043 ± 0.008‡	101 ± 5.1	0.91 ± 0.01
	Spitzer LL	96.7 ± 1.2‡	0.043 ± 0.008‡	95.8 ± 4.8	0.91 ± 0.01
1702 Kalahari	Spitzer SL	34.6 ± 0.1‡	0.065 ± 0.008‡	34.7 ± 1.7	0.85 ± 0.01
	Spitzer LL	34.6 ± 0.1‡	0.065 ± 0.008‡	33.7 ± 1.7	0.75 ± 0.01
3552 Don Quixote	Spitzer LL	19.0	0.030	18.7 ± 0.9	0.76 ± 0.01

Note. For each asteroid, the literature values for diameter and albedo were taken from JPL Horizons. Observations marked with † are based on IRAS data (Tedesco et al. 2004), and those marked with ‡ are based on NEOWISE (Mainzer et al. 2019) measurements. The diameter and albedo values cited in the JPL Horizons database for 190 Ismene were sourced from personal communication with J. G. Williams and did not have associated error estimates. Similarly, the diameter and albedo values of 944 Hidalgo and 3552 Don Quixote were sourced from Gehrels (1994) and also did not include error estimates. Note that a lack of contemporaneous photometry for the June G227 observations of 46 Hestia (starred) resulted in a fit with an asteroid diameter that does not agree with the literature values, as these observations could not be scaled to account for potential slit losses.

wavelengths shorter than the midpoint of the bounds, whereas a right-skewing feature has a skew of >0.5 , indicating that the continuum-removed peak falls at wavelengths longer than the midpoint of the bounds. For example, the skew of 87 Sylvia is 0.44, indicating that the peak of the $10\ \mu\text{m}$ feature occurs just shortward of the midpoint of the continuum line (see Figure 5). Note that this method for measuring skew matches the one described for measuring the skew of laboratory spectra in Martin et al. (2022) but is different from the one that Martin & Emery (2023) use to measure the skew of asteroid spectra.

All the asteroids we examine are skewed toward shorter wavelengths; that is, they have skews of <0.5 . We also note that for many of the asteroids in our sample, the continuum slopes are flat; this is in contrast with the Trojans in Martin & Emery (2023), which in general have positive slopes (e.g., increasing emissivity with increasing wavelength). 944 Hidalgo, 1268 Libya, and 1702 Kalahari are exceptions to this general trend; these asteroids all have positive continuum slopes significant at the 1σ level. We do not see any asteroids with statistically significant negative continuum slopes. In terms of spectral contrast, the contrasts we calculate are comparable to those seen in the Trojans (Licandro et al. 2011; Martin & Emery 2023).

4. Discussion

To identify the mineralogies present on the surfaces of these asteroids, we follow the approach of Martin & Emery (2023).

That work used the characteristic wavelengths of individual peaks and dips superimposed on the broad $10\ \mu\text{m}$ silicate emission feature to argue that the spectra of a collection of Trojans showed evidence of the presence of forsteritic olivine and enstatite (pyroxene). Martin et al. (2022, 2023) also demonstrated that while the spectral contrast of diagnostic silicate features varies with regolith porosity, the locations of many features in wavelength space do not vary. Therefore, these features can be used to identify silicate mineralogy independently of regolith porosity, with the appearance of multiple peaks associated with the same mineral interpreted as strong evidence of the presence of that mineral in the asteroid's spectrum. In addition to using the laboratory studies of Martin et al. (2022, 2023), we also employ previous work including laboratory measurements of the absorption coefficients of olivines and pyroxenes (e.g., Koike et al. 1993, 2003; Chihara et al. 2002). To compare the absorption coefficients measured in those papers and the emission features considered in this work, we make the following assumptions. First, we assume that the contribution of surface scattering to the spectral appearance of the asteroids in our sample is negligible, as evidenced by the appearance of the $10\ \mu\text{m}$ feature in emission and the lack of a Christiansen feature, both of which are associated with the transition from the primarily surface-scattering regime to the volume-scattering regime (Martin et al. 2022, 2023). We also assume that we can relate emission and absorption features according to Kirchhoff's law, an assumption commonly used among laboratory studies of mid-IR spectroscopy (e.g., Salisbury et al. 1991) that predicts that the positions of spectral features are unchanged when considered in terms of emissivity rather than reflectance. Like Martin &

Table 5
Location of Common Spectral Features

Asteroid	$D_{5.5}$ (μm)	P_6 (μm)	D_7 (μm)	$P_{7.5}$ (μm)	D_8 (μm)	P_9/S_9 (μm)	P_{10} (μm)
46 Hestia	-	-	-	-	-	$9.06 \pm 0.01^*$	-
65 Cybele	5.68 ± 0.09	5.97 ± 0.01	6.88 ± 0.06	7.38 ± 0.10	7.90 ± 0.10	X	9.73 ± 0.05
87 Sylvia	5.77 ± 0.06	6.04 ± 0.06	6.62 ± 0.16	7.54 ± 0.06	7.80 ± 0.04	9.15 ± 0.05	9.56 ± 0.02
140 Siwa	5.73 ± 0.02	5.95 ± 0.01	6.77 ± 0.17	7.46 ± 0.07	X*	$9.14 \pm 0.24^*$	X*
190 Ismene	-	-	-	-	-	$9.12 \pm 0.02^*$	-
267 Tirza	5.81 ± 0.03	6.02 ± 0.01	7.08 ± 0.03	X	7.80 ± 0.10	9.35 ± 0.03	9.84 ± 0.15
269 Justitia	5.78 ± 0.03	6.72 ± 0.08	7.00 ± 0.05	X	7.85 ± 0.02	X	9.66 ± 0.13
336 Lacadiera	5.65 ± 0.12	5.95 ± 0.07	6.60 ± 0.12	7.51 ± 0.09	7.63 ± 0.08	9.14 ± 0.10	9.77 ± 0.06
368 Haidea	X	X	6.69 ± 0.01	7.59 ± 0.08	8.18 ± 0.05	9.26 ± 0.02	10.55 ± 0.08
944 Hidalgo	5.66 ± 0.04	5.93 ± 0.04	6.52 ± 0.05	7.20 ± 0.04	7.41 ± 0.06	9.20 ± 0.04	9.85 ± 0.19
1268 Libya	X	X	6.82 ± 0.19	7.43 ± 0.01	7.74 ± 0.03	X	10.3 ± 0.14
1702 Kalahari	X	X	7.07 ± 0.01	7.52 ± 0.05	7.99 ± 0.04	9.66 ± 0.08	10.3 ± 0.17
3552 Don Quixote	-	-	-	-	-	-	-
Feature Description	Sharp Dip	Plateau	Dip	Plateau	Low Bound of 10 μm Feature	Shoulder Minor Peak	Peak of 10 μm Feature
Asteroid	P_{11}/S_{11} (μm)	$D_{12.5}$ (μm)	P_{13} (μm)	$P_{14.5}$ (μm)	P_{17} (μm)	P_{20} (μm)	Shape of 10 μm Feature
46 Hestia	X*	X*	X*	-	-	$20.74 \pm 0.57^*$	X
65 Cybele	11.68 ± 0.12	12.27 ± 0.07	13.30 ± 0.04	14.23 ± 0.03	17.66 ± 0.01	-	Trapezoidal
87 Sylvia	11.2 ± 0.07	12.03 ± 0.11	12.63 ± 0.03	15.00 ± 0.31	17.39 ± 0.35	20.13 ± 0.45	Trapezoidal
140 Siwa	$10.9 \pm 0.09^*$	$12.45 \pm 0.11^*$	$11.91 \pm 0.15^*$	-	-	$20.07 \pm 0.46^*$	Present
190 Ismene	X?*	X?*	X?*	-	-	X*	X?
267 Tirza	11.23 ± 0.07	12.67 ± 0.10	12.97 ± 0.03	14.33 ± 0.04	16.7 ± 0.06	18.97 ± 0.21	Trapezoidal
269 Justitia	11.72 ± 0.07	12.82 ± 0.07	X	-	-	-	Rounded
336 Lacadiera	11.5 ± 0.03	11.97 ± 0.11	12.51 ± 0.12	-	-	-	Rounded
368 Haidea	X	12.18 ± 0.04	12.64 ± 0.21	14.76 ± 0.08	16.93 ± 0.718	X	Rounded
944 Hidalgo	11.12 ± 0.04	12.28 ± 0.06	12.88 ± 0.04	X	16.47 ± 0.07	19.38 ± 0.06	Trapezoidal
1268 Libya	11.49 ± 0.05	12.30 ± 0.04	13.00 ± 0.08	14.27 ± 0.01	X	19.14 ± 0.06	Rounded
1702 Kalahari	11.5 ± 0.16	12.27 ± 0.05	12.93 ± 0.15	15.11 ± 0.30	17.93 ± 0.85	X	Rounded
3552 Don Quixote	-	-	-	-	16.44 ± 0.53	20.65 ± 0.01	-
Feature Description	Shoulder or Minor Peak	High Bound of 10 μm Feature	Minor Peak	Peak	Broad Peak	Broad Peak	

Note. Positions and locations of various features common to the mid-IR spectra of the asteroids analyzed. Measurements are based on the Spitzer Space Telescope, except those marked with an asterisk, which indicates observations from the SOFIA spectra. The letters P, D, and S indicate whether the feature is a peak, dip, or shoulder, while the corresponding number gives the *approximate* position of the feature. Each feature is also briefly described. An X indicates the feature was not present in the spectrum, while a dash indicates there was no coverage of the relevant wavelength region. The X? symbol, used only for 190 Ismene, indicates that while this wavelength region was covered, systematic issues in the spectrum complicate the interpretation of individual features.

Emery (2023), we assume the emission features we observe are linearly additive—that is, that the characteristic features of olivine and pyroxene mixtures can be identified by their diagnostic peaks superimposed on the broader 10 and 20 μm peaks.

We identify crystalline olivine, amorphous olivine, crystalline pyroxene, and amorphous pyroxene as likely majority components contributing to the overall appearance of the 10 and 20 μm silicate emission features. Both olivine and pyroxene are names given to classes of silicate minerals that can exhibit varying bulk proportions of Mg and Fe in solid solution. For olivine, forsterite refers to the the Mg-rich end-member, and for fayalite, it refers to the Fe-rich end-member. For pyroxene, the Mg-rich end-member is enstatite, and the Fe-rich end-member is ferosilite. In general, unless otherwise noted, we use the spectra of the magnesium-rich end-members

for each silicate. Our choice to use the magnesium-rich end-members was influenced by the observation that increasing Mg# in both olivine and pyroxene tends to shift individual features to shorter wavelengths (e.g., Chihara et al. 2002; Koike et al. 2003). As the spectral features of the asteroids we examined in this paper tend to skew toward shorter wavelengths, we selected the most magnesium-rich olivine or pyroxene available with sufficient resolution in the 10 μm region to be our example end-member. Martin & Emery (2023) also explore how the addition of silicates with lower Mg# acts to change the skew of the 10 μm feature as applied to the spectrum of 617 Patroclus–Menoetius. We produce simple linear mixture models using these four silicates to explore how the inclusion of these components affects the spectral shapes of the 10 and 20 μm silicate emission features and provide a visual comparison between these silicate mixtures and the

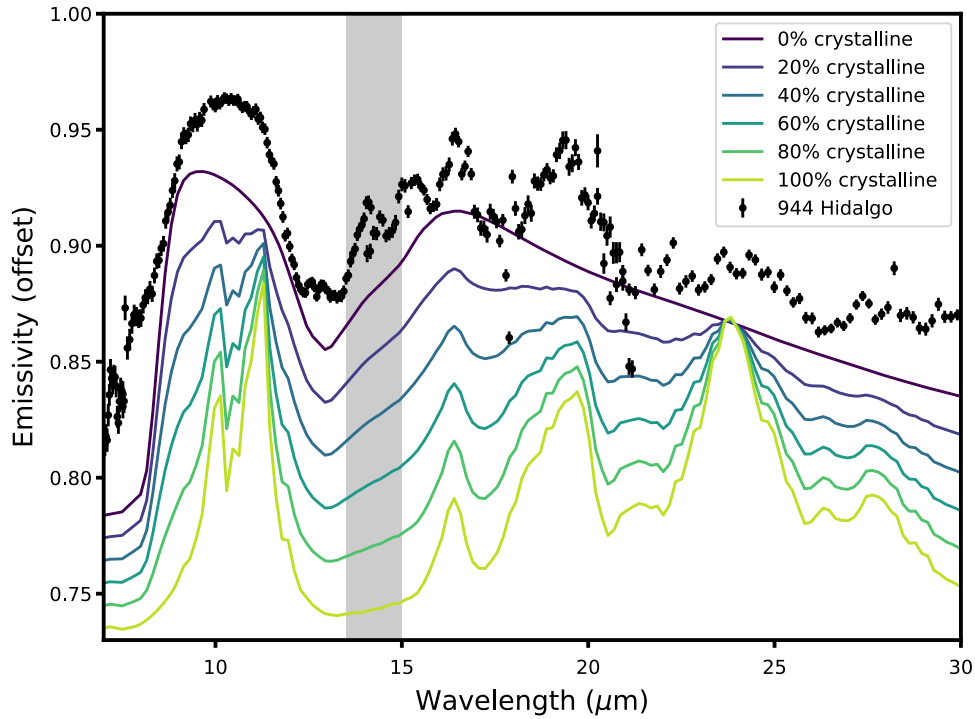


Figure 6. Modeled mixtures of magnesium-rich crystalline and amorphous olivine compared to the spectrum of 944 Hidalgo. Increasing the proportion of amorphous olivine in these mixtures dampens the spectral contrast of the smaller peaks superimposed on the 10 μm silicate plateau, suggesting a high proportion of amorphous silicates among the asteroids observed with Spitzer and SOFIA. The shaded gray box highlights the location of a known artifact in the SL Spitzer data (the SL teardrop). Spectra of crystalline silicates are sourced from Chihara et al. (2002) and Koike et al. (2003), and spectra of amorphous silicates are derived from optical constants from Jäger et al. (1994, 2003) and Dorschner et al. (1995) (see text for modeling details and silicate compositions).

Table 6
Characterization of the 10 μm Feature

Asteroid	Width (μm)	Continuum Slope (Emissivity/ μm)	Continuum-removed Peak (μm)	Skew	Spectral Contrast (%)
65 Cybele	4.37 ± 0.12	0.001 ± 0.002	9.68 ± 0.04	0.41 ± 0.07	5.8 ± 0.6
87 Sylvia	4.23 ± 0.12	0.003 ± 0.001	9.68 ± 0.14	0.44 ± 0.10	6.1 ± 0.6
267 Tirza	4.87 ± 0.14	0.005 ± 0.005	9.81 ± 0.15	0.41 ± 0.09	12 ± 2.0
269 Justitia	4.87 ± 0.07	0.002 ± 0.001	9.64 ± 0.15	0.36 ± 0.09	5.1 ± 0.8
336 Lacadiera	4.34 ± 0.14	0.001 ± 0.003	9.63 ± 0.17	0.46 ± 0.11	4.6 ± 0.9
368 Haidea	3.9 ± 0.06	0.004 ± 0.005	9.26 ± 0.02	0.25 ± 0.06	6.5 ± 2.1
944 Hidalgo	4.87 ± 0.08	0.009 ± 0.002	9.81 ± 0.17	0.49 ± 0.08	11 ± 0.7
1268 Libya	4.56 ± 0.05	0.010 ± 0.002	9.61 ± 0.26	0.41 ± 0.14	6.7 ± 0.7
1702 Kalahari	4.63 ± 0.05	0.014 ± 0.004	9.43 ± 0.12	0.39 ± 0.07	7.3 ± 1.8

Note. Band parameters of the 10 μm feature. Band parameters are measured as described in Martin & Emery (2023), except for skew (see text).

asteroid spectra considered in this work (Figures 6 and 7). To generate these mixing models, we model the predicted emission for amorphous silicates starting from the optical constants for a silicate grain with a radius of 5 μm following the methods of Lisse et al. (2006). We used optical constants reported in Jäger et al. (1994) and Dorschner et al. (1995) for amorphous olivine ($\text{Mg}\# = 1.0$) and Jäger et al. (2003) for amorphous pyroxene ($\text{Mg}\# = 0.95$). For crystalline silicates, we use data from Chihara et al. (2002) and Koike et al. (2003) for forsteritic olivine ($\text{Mg}\# = 1.0$) and ortho-enstatite pyroxene ($\text{Mg}\# = 1.0$), respectively. The iron-rich end-members considered in the discussion of 368 Haidea are 1:1 mixtures of amorphous and crystalline silicates with $\text{Mg}\# = 0.4$ for the amorphous silicates (the lowest $\text{Mg}\#$ measured in Jäger et al.

1994, 2003; Dorschner et al. 1995) and $\text{Mg}\# = 0.0$ for the crystalline silicates (Chihara et al. 2002; Koike et al. 2003).

We then produced linear mixtures of the emission spectra of the spectral end-members to create a synthetic spectrum. The resulting synthetic emission spectrum was then scaled as in Martin & Emery (2023) to match the spectral contrast of the mixture model to the spectral contrast of the 10 μm emission feature in the asteroid spectra. These simplified models do not account for all the complexities inherent to asteroidal surfaces, including grain size distributions and the addition of nonsilicate components, but are used here to illustrate a few key principles contributing to our analysis of the silicate mineralogy of the asteroids.

Following these principles, our results suggest mineralogical similarities between the Trojans and D- and P-types in the main

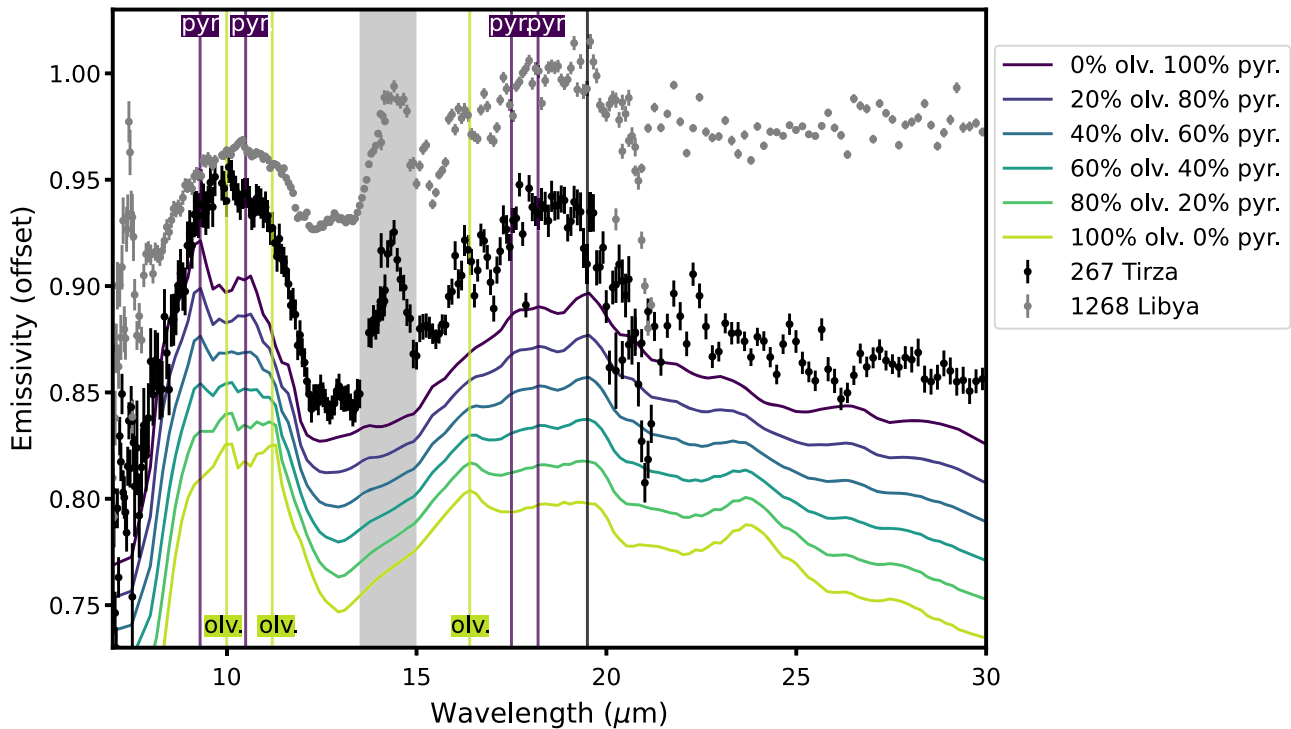


Figure 7. Modeled mixtures of magnesium-rich pyroxenes and olivines plotted alongside the spectrum of 267 Tirza and 1268 Libya. The addition of pyroxene to the olivine mixtures changes the behavior of the spectrum at long wavelengths, broadening this emission feature from the distinct emission peak(s) seen in the spectra of olivine and pyroxene alone. Spectral features of olivine are marked in light green, and those of pyroxenes are marked in dark purple to highlight commonalities with the asteroid spectra. The feature at $19.5\ \mu\text{m}$ is common to both olivine and pyroxene. The spectrum of 267 Tirza in particular shows evidence of both olivine and pyroxene. All mixtures shown here contain both amorphous and crystalline silicates mixed in a 3:1 ratio, while the proportion of olivine and pyroxene is varied. The shaded gray box highlights the location of a known artifact in the SL Spitzer data (the SL teardrop). Spectra of crystalline silicates are sourced from Chihara et al. (2002) and Koike et al. (2003), and spectra of amorphous silicates are derived from optical constants from Jäger et al. (1994, 2003) and Dorschner et al. (1995) (see text for modeling details and silicate compositions).

belt. In particular, the peak or shoulder between 11.2 and $11.4\ \mu\text{m}$ is associated with crystalline olivine, with the range of feature positions associated with the different Mg# within the crystal structure of olivine (Koike et al. 1993, 2003). Like Martin & Emery (2023), we take the presence of the $11\ \mu\text{m}$ features as evidence for the presence of olivine. In the long-wavelength region, olivines show additional structure including a broad peak from 16 to $17\ \mu\text{m}$, a broad peak from 19 to $20\ \mu\text{m}$, and a peak near $24\ \mu\text{m}$. The spectrum of 944 Hidalgo shows strong evidence of the presence of olivine with the presence of these peaks in the $20\ \mu\text{m}$ regions (see Figure 6).

For some asteroids in our sample, there is evidence of pyroxenes contributing to the shapes of the 10 and $20\ \mu\text{m}$ silicate emission features. While the spectrum of 944 Hidalgo shows the olivine silicate peaks near $20\ \mu\text{m}$ most clearly, these peaks are less clear for 267 Tirza and 1268 Libya, which instead have a broad emission feature peaking near $19\ \mu\text{m}$. This broad peak may be due to the presence of pyroxene either alone or in combination with olivine. Some pyroxenes, particularly amorphous pyroxenes, show a prominent and broad long-wavelength peak between 19 and $20\ \mu\text{m}$ (Brucato et al. 1999; Chihara et al. 2002) consistent with the interpretation that there is evidence of pyroxene in the spectra of 267 Tirza and 1268 Libya. At short wavelengths, 267 Tirza shows additional evidence of pyroxene via a $9.3\ \mu\text{m}$ peak associated with pyroxene (Chihara et al. 2002) along with the $11.2\ \mu\text{m}$ peak that we attribute to olivine. 1268 Libya also shows evidence of pyroxenes at short wavelengths with a prominent peak at $10.5\ \mu\text{m}$ and a smaller peak near $11.5\ \mu\text{m}$ (Chihara et al. 2002),

though the latter can also be interpreted as evidence for fayalitic olivine, which has a peak near $11.4\ \mu\text{m}$ (Koike et al. 2003). Thus, a mixture of olivines and pyroxenes may be able to simultaneously account for the features in the 10 and $20\ \mu\text{m}$ regions of the spectra of 267 Tirza and 1268 Libya.

In general, the emissivity spectra of crystalline silicates are sharper and more distinct than their amorphous counterparts (e.g., Hallenbeck et al. 1998; Brucato et al. 1999). Spectral mixing models predict that increasing the proportion of amorphous olivines and pyroxenes in a mixture acts to dampen the distinctiveness of individual silicate emissivity peaks and to round the overall shape of the $10\ \mu\text{m}$ plateau (see Figure 6 of this paper and Figure 6 of Martin & Emery 2023). While we can identify individual silicate peaks and shoulders superimposed on the broad $10\ \mu\text{m}$ plateau, the spectral contrasts of these features are much smaller than would be expected of a purely crystalline composition, evidence that a high proportion of the silicates on the surfaces of these asteroids are amorphous, particularly among the asteroids classified as having “rounded” $10\ \mu\text{m}$ features (e.g., 336 Lacadiera, 1268 Libya, and 1702 Kalahari). We also see evidence of amorphous silicates on the surfaces of many asteroids in our sample, in particular, with the presence of a very broad peak near $9.8\ \mu\text{m}$ (particularly in continuum-removed space) of amorphous silicates that is also found in Trojan spectra (Emery et al. 2006; Martin & Emery 2023).

In general, we see many commonalities in the mid-infrared spectra of the D- and P-type asteroids in our sample and the Trojans. We see evidence of the $10\ \mu\text{m}$ silicate emission

features in the spectra of all the asteroids we examined, with the exception of 46 Hestia. While 46 Hestia lacks evidence of a $10\ \mu\text{m}$ feature, we note emission features in the $20\ \mu\text{m}$ region that may be due to silicates. In both the Trojans (Martin & Emery 2023) and our sample, we see these features exhibiting both rounded and trapezoidal shapes. The range of spectral contrasts of these features is also comparable to the range of contrasts exhibited by the Trojans: 624 Hektor has an estimated spectral contrast of $\sim 15\%$ (Licandro et al. 2011), and 617 Patroclus has a spectral contrast of $\sim 4\%$ (Martin & Emery 2023), while our sample spans contrasts from 4% to 17%. Since the spectral contrast of the $10\ \mu\text{m}$ feature is associated with high regolith porosity (Martin et al. 2022, 2023), this finding implies similar regolith surface properties on both Trojans and main-belt asteroids. Previous authors have suggested the suspension of regolith particles within a “fairy-castle” structure (Emery et al. 2006; Mueller et al. 2010) or transparent (in the mid-IR) matrix (Yang et al. 2013; Sultana et al. 2023) to explain the emission features of Jupiter Trojans. Our results suggest that these mechanisms are also relevant to the surfaces of D- and P-type asteroids outside of the Trojan population. Other features our spectra have in common with the Trojans examined in Martin (2022) include the small emissivity peak at $13\ \mu\text{m}$ (e.g., 87 Sylvia, 65 Cybele, and 944 Hidalgo) in the overall emissivity dip between 12 and $14\ \mu\text{m}$, though these features were not attributed to any particular silicate composition.

However, there are some slight differences between the main-belt sample presented here and the spectra of the Trojans in Martin & Emery (2023) in terms of the shape of the $10\ \mu\text{m}$ feature; our main-belt asteroids have flatter continuum slopes and skew to shorter wavelengths, though we note that the measured continuum slope is dependent on the results of the thermal modeling process. The leftward (e.g., toward shorter wavelengths) skew of the $10\ \mu\text{m}$ plateau among the asteroids in our sample also contrasts with the Trojans, which skew rightward (e.g., toward longer wavelengths). In Martin & Emery (2023), the rightward-skewing $10\ \mu\text{m}$ feature of the Trojans is noted as a major difference between both spectral mixture models of crystalline and amorphous olivines and pyroxenes as well as simulated emission spectra derived from meteoritic analogs in the ASTER spectral library (Baldrige et al. 2009; Martin 2022). In that work, Martin (2022) suggests that the rightward skews of Trojan $10\ \mu\text{m}$ emission plateaus could be caused by an additional spectral component responsible for muting the short-wavelength silicate peaks. In contrast, the leftward skews of the $10\ \mu\text{m}$ features of asteroids in our main-belt sample indicate that the currently unknown physical mechanism responsible for skewing the $10\ \mu\text{m}$ feature of Trojans to longer wavelengths is not relevant to the asteroids in this sample.

In Martin & Emery (2023), the VNIR spectral slope was found to be correlated with the spectral contrast of the $10\ \mu\text{m}$ feature among the Jupiter Trojans. Therefore, we might expect the objects in our sample with redder spectral slopes, e.g., the D-types (267 Tirza, 336 Lacadiera, 368 Haidea, 944 Hidalgo, and 1702 Kalahari) and 269 Justitia, to have high spectral contrasts. While the asteroids with the three highest spectral contrasts (944 Hidalgo, 267 Tirza, and 1702 Kalahari) are all D-types (Neese 2017), the more moderate spectral contrasts of 336 Lacadiera, 368 Haidea, and 269 Justitia do not align with this expectation. In particular, 269 Justitia’s exceptionally red

NIR ($0.7\text{--}2.5\ \mu\text{m}$) slope of $9\%/100\ \text{nm}$ (Hasegawa et al. 2021) exceeds the $5\%/100\ \text{nm}$ NIR slopes of the average R-group Trojan (Emery et al. 2010). Therefore, if Justitia followed the trend observed in Martin & Emery (2023), we would expect it to have a prominent $10\ \mu\text{m}$ feature, but its spectral contrast is comparable to the more moderately sloped P-types. Hasegawa et al. (2021) hypothesize that 269 Justitia’s extremely red spectral slope in the VNIR suggests that this asteroid originated from the 20–30 au region. Similarly, Martin & Emery (2023) suggest a cometary or Kuiper Belt origin for the Trojans based on their spectral similarity to comets. 269 Justitia’s $10\ \mu\text{m}$ emission feature resembles the rounded $10\ \mu\text{m}$ emission features of some Trojans, particularly the more moderately sloped LR Trojans (e.g., 617 Patroclus–Menoetius in Mueller et al. 2010; Martin & Emery 2023), supporting a common distant outer solar system origin for both 269 Justitia and the Trojans. However, the spectrum of 269 Justitia shows additional spectral structure (a series of peaks and dips from 7.5 to $10\ \mu\text{m}$ superimposed on the short-wavelength $10\ \mu\text{m}$ shoulder) not seen among the Trojans, potentially indicating an additional compositional component present on 269 Justitia that is absent from the Trojans. These features, as well as the low spectral contrast of 269 Justitia’s $10\ \mu\text{m}$ feature, complicate the interpretation that 269 Justitia and the Trojans are sourced from the same population.

We note that two of the D-types in our sample, 944 Hidalgo and 3552 Don Quixote, are unique among our sample population for their high eccentricities ($e > 0.5$) and semimajor axes ($a > 4.0\ \text{au}$). Both 944 Hidalgo and 3552 Don Quixote are extinct comet candidates, with 3552 Don Quixote likely originating from the Jupiter-family comet (JFC) population (Weissman et al. 2002). The spectra of 944 Hidalgo and 3552 Don Quixote also resemble those of 10P/Tempel 2 and 49P/Arend–Rigaux, two JFCs, with their 10 and $20\ \mu\text{m}$ silicate emission features (Kelley et al. 2017). The resemblance of the mid-infrared spectrum of 3552 Don Quixote to comets has also been noted in Mommert et al. (2014). That paper also noted evidence of cometary activity on 3552 Don Quixote, including a coma and tail. The resemblance of 944 Hidalgo and 3552 Don Quixote to comet populations in the mid-infrared lends support to the hypothesis that these objects originated in cometary populations.

The spectrum of 368 Haidea represents an exception to the trends described above. The spectrum of 368 Haidea lacks strong evidence of the presence of olivine due to the absence of a peak or shoulder at $11\ \mu\text{m}$. 368 Haidea’s continuum-removed peak is also shifted to shorter wavelengths, resulting in a notably low value for skew (see Table 6). Martin et al. (2022) showed that the appearance of a strong $11\ \mu\text{m}$ feature is characteristic of olivines and appears in laboratory spectra of olivines regardless of regolith porosity. Therefore, while 368 Haidea has a relatively modest spectral contrast compared to other asteroids in our sample, we should still expect to see an $11\ \mu\text{m}$ feature if the asteroid had an olivine-rich composition, as the appearance of this feature is independent of porosity. While 368 Haidea’s $10\ \mu\text{m}$ plateau feature has a relatively low spectral contrast, its spectral shape in the $10\ \mu\text{m}$ region is distinct from other asteroids in our sample with similar spectral contrasts that do show evidence of features at $11\ \mu\text{m}$ (e.g., 87 Sylvia and 1268 Libya). Therefore, we disfavor the explanation that the lack of an $11\ \mu\text{m}$ feature is due to a difference in regolith porosity.

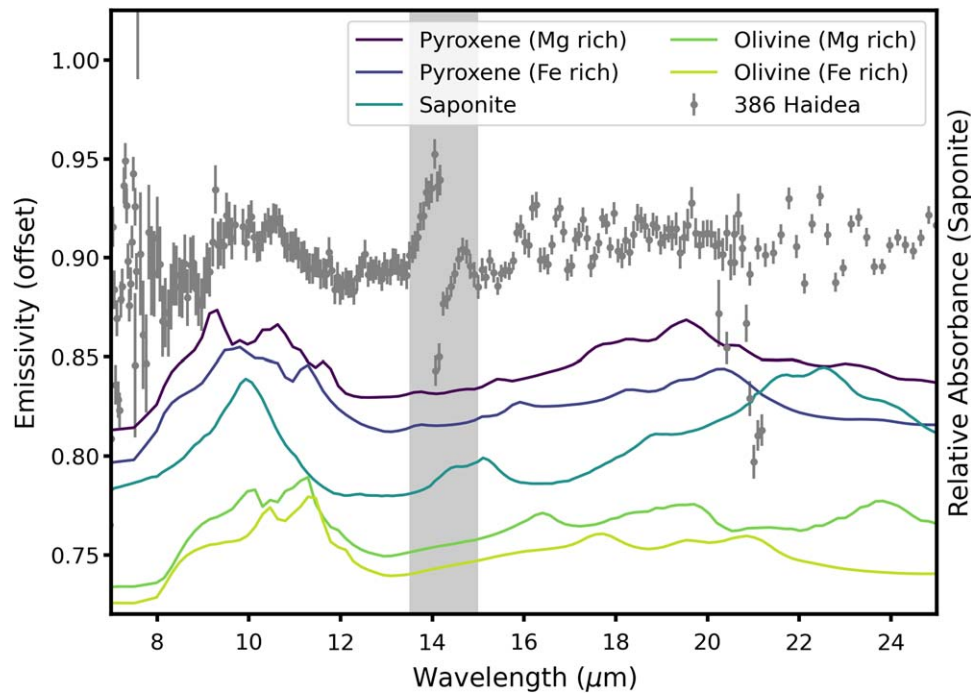


Figure 8. 386 Haidea is distinguished from other asteroids in our sample by its shortward skew and lack of an 11 μm olivine shoulder, which could be due to a relatively olivine-poor composition. The 10 μm plateau in the pyroxene and phyllosilicate spectra is also skewed to shorter wavelengths and provides a closer match to the shape of 368 Haidea's 10 μm feature than either forsteritic or fayalitic olivine does. Either of these minerals may be able to account for 386 Haidea's unusual spectrum and could point to a geochemical history different from the olivine-dominated spectra of the other asteroids in our sample. Pyroxene and olivine spectra are modeled as 1:1 mixtures of amorphous and crystalline silicates based on optical constants from Jäger et al. (1994, 2003), Dorschner et al. (1995), and Chihara et al. (2002). The saponite spectrum is measured in relative absorbance as derived by Beck et al. (2014) via measurements originally made by Salisbury et al. (1991). The shaded gray box highlights the location of a known artifact in the SL Spitzer data (the SL teardrop). Spectra of crystalline silicates are sourced from Chihara et al. (2002) and Koike et al. (2003), and spectra of amorphous silicates are derived from optical constants from Jäger et al. (1994, 2003) and Dorschner et al. (1995) (see text for modeling details and silicate compositions).

The difference in spectral shape may be due to a difference in composition. 368 Haidea's strongest peaks are located at 9.2 and 10.5 μm , both prominent peaks associated with pyroxenes, particularly enstatite (Chihara et al. 2002), which could be interpreted as evidence for a pyroxene-rich composition. Increasing pyroxene content can also explain the shortward skew of 368 Haidea's 10 μm plateau (the effect of introducing pyroxenes is also demonstrated in Figure 7). However, shortward shifts of the 10 μm feature, in concert with weakening 11 μm olivine features, have also been associated with increasing degrees of aqueous alteration in meteorites, leading to the alternative conclusion that 368 Haidea may be hydrated (Beck et al. 2014). As that paper shows, hydrated silicates (in meteorites) can still have quite prominent 10 μm features, with hydrated minerals often showing a feature near 10 μm . The hydrated silicate interpretation is supported by the spectral similarity (in the VNIR and mid-IR) of 368 Haidea to the Tagish Lake meteorite noted in Vernazza et al. (2013). The Tagish Lake meteorite has been shown to have widespread evidence of aqueously altered minerals, including phyllosilicates (Zolensky et al. 2002; Gilmour et al. 2019). Spectra of pyroxenes and the phyllosilicate saponite more closely resemble the spectrum of 368 Haidea than the spectrum of olivine (see Figure 8). Both iron-rich and magnesium-rich olivines do not provide a close spectral match to 368 Haidea; the addition of iron-rich olivine (fayalite) in particular skews the 10 μm feature to even longer wavelengths than forsterite and provides a poorer match. While the pyroxene-rich and phyllosilicate-rich interpretations of 368 Haidea imply different geochemical histories for this asteroid, the lack of evidence for

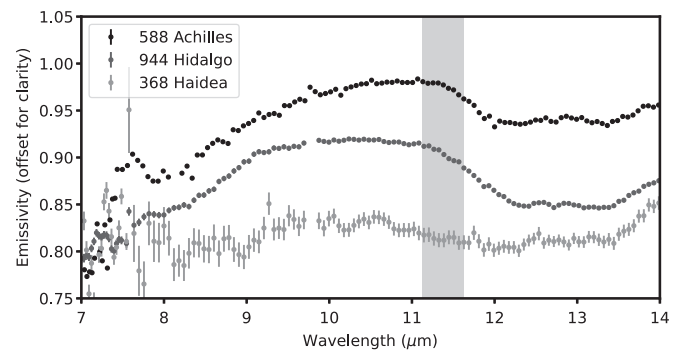


Figure 9. Comparison of the spectra of 588 Achilles from Martin & Emery (2023) to 944 Hidalgo and 368 Haidea (this study). In the VNIR, 588 Achilles, 944 Hidalgo, and 368 Haidea are all classified as D-types and have similar albedos, yet 368 Haidea lacks a strong peak or shoulder in the 11 μm region indicative of olivine (see highlighted region). Comparing the spectra of 944 Hidalgo and 588 Achilles, we can also see how the asteroids examined in this work have shallower continuum slopes and more leftward-skewed 10 μm features than the Trojans in Martin & Emery (2023).

olivine features in the mid-infrared spectrum of 368 Haidea clearly distinguishes it from the Trojans (see Figure 9).

Overall, we see that the majority of the primitive asteroids in our sample, with the exception of 368 Haidea, resemble both each other and the Trojans. The similarity in spectral shape of the 10 μm features extends to a similarity in both anhydrous silicate composition (olivine and pyroxene mixtures) and high regolith porosity. Asteroids that resemble the Trojans in this way include both D- and P-types. Some major divergences from the spectra of the asteroids examined in this paper and

previously published Trojan spectra are the lower continuum slopes and leftward skews of the $10\ \mu\text{m}$ features seen in our sample. In the Trojans, the $10\ \mu\text{m}$ feature tends to have a continuum slope that increases steeply with increasing wavelength and rightward-skewing $10\ \mu\text{m}$ features (Martin & Emery 2023). The mineralogical significance of these spectral differences, however, is unclear.

The distinctive spectrum of 368 Haidea is distinguished from the other asteroids in our sample and the Trojans (Emery et al. 2006; Martin & Emery 2023) by the lack of evidence of spectral features associated with olivine, particularly the $11\ \mu\text{m}$ peak. 368 Haidea is also notable for its low skew of 0.25. The shortward shift of 368 Haidea's features may be due to a particularly pyroxene- or phyllosilicate-rich composition, suggesting that 368 Haidea does not originate from the same source populations as the Trojans and other main-belt D-types. Comparing 368 Haidea to the other D-types in our sample demonstrates the need for observations outside of the VNIR region, particularly for asteroids with few spectral features in the VNIR, to augment our understanding of the compositions of these asteroids. The recently launched JWST will be able to extend mid-infrared observations to a larger population of primitive asteroids, sampling cooler and fainter populations of primitive small solar system bodies and supplementing our understanding of ground-based VNIR asteroid taxonomies.

5. Conclusions





Combining new observations from SOFIA and archival data from the Spitzer Space Telescope, we examine the mid-infrared ($5\text{--}40\ \mu\text{m}$) spectra of 13 primitive main-belt D- and P-type asteroids. While these two asteroid populations resemble each other in the VNIR, a lack of strong spectral features in the VNIR limits the extent to which we can unambiguously determine their compositions. We analyze the spectra of these asteroids, including using techniques to characterize the $10\ \mu\text{m}$ region developed in Martin & Emery (2023), to compare the composition and regolith properties of D- and P-types in the main belt to the Jupiter Trojans. We find that the majority of D- and P-type main-belt asteroids in our sample resemble the Trojans in the mid-IR, with high regolith porosities and a silicate composition incorporating crystalline and amorphous olivines and pyroxenes, suggesting a common origin for primitive asteroids in the main-belt and Trojan swarms. However, we also note some differences in the general shapes of the $10\ \mu\text{m}$ features of main-belt and Trojan asteroids, including lower continuum slopes and leftward-skewing $10\ \mu\text{m}$ emission features among main-belt asteroids as compared to Trojans. In addition, we identify a D-type asteroid, 368 Haidea, that is distinguished from both the Trojans and main-belt asteroids in our sample by a spectrum lacking the $11\ \mu\text{m}$ olivine-related emission feature. Despite their shared D-type classification, 368 Haidea does not resemble D-type Jupiter Trojans, suggesting that similarity in VNIR spectra does not guarantee a shared surface composition as reflected by silicate features in the mid-infrared.

Acknowledgments

The authors would like to thank Dr. Maggie McAdam for her assistance in preparing the SOFIA proposal. The authors would also like to thank the two anonymous reviewers whose input greatly improved the clarity of the manuscript. This work

is based in part on observations made with the NASA/DLR Stratospheric Observatory for Infrared Astronomy (SOFIA). SOFIA is jointly operated by the Universities Space Research Association, Inc. (USRA), under NASA contract NNA17BF53C and the Deutsches SOFIA Institut (DSI) under DLR contract 50 OK 2002 to the University of Stuttgart. Financial support for this work was provided by NASA through award No. 08-0105 issued by USRA. This work is based in part on archival data obtained with the Spitzer Space Telescope, which was operated by the Jet Propulsion Laboratory, California Institute of Technology, under a contract with NASA. This research has made use of data and/or services provided by the International Astronomical Union's Minor Planet Center. The majority of this work was completed at Northern Arizona University in Flagstaff, Arizona. Northern Arizona University sits at the base of the San Francisco Peaks, on homelands sacred to Native Americans throughout the region. We honor their past, present, and future generations, who have lived here for millennia and will forever call this place home.

ORCID iDs

Oriel A. Humes  <https://orcid.org/0000-0002-1700-5364>
 Audrey C. Martin  <https://orcid.org/0000-0003-3402-1339>
 Cristina A. Thomas  <https://orcid.org/0000-0003-3091-5757>
 Joshua P. Emery  <https://orcid.org/0000-0001-9265-9475>

References

- Baldrige, A. M., Hook, S. J., Grove, C., & Rivera, G. 2009, *RSEnv*, **113**, 711
- Beck, P., Garenne, A., Quirico, E., et al. 2014, *Icar*, **229**, 263
- Binzel, R. P., Rivkin, A. S., Stuart, J. S., et al. 2004, *Icar*, **170**, 259
- Brucato, J., Colangeli, L., Mennella, V., Palumbo, P., & Bussolotti, E. 1999, *A&A*, **348**, 1012
- Chihara, H., Koike, C., Tsuchiyama, A., Tachibana, S., & Sakamoto, D. 2002, *A&A*, **391**, 267
- Decin, L., Morris, P., Appleton, P., et al. 2004, *ApJS*, **154**, 408
- DeMeo, F., & Carry, B. 2013, *Icar*, **226**, 723
- DeMeo, F. E., Binzel, R. P., Carry, B., Polishook, D., & Moskovitz, N. A. 2014, *Icar*, **229**, 392
- DeMeo, F. E., Binzel, R. P., Slivan, S. M., & Bus, S. J. 2009, *Icar*, **202**, 160
- Dorschner, J., Begemann, B., Henning, T., Jaeger, C., & Mutschke, H. 1995, *A&A*, **300**, 503
- Emery, J., & Brown, R. 2004, *Icar*, **170**, 131
- Emery, J., Cruikshank, D., & Van Cleve, J. 2006, *Icar*, **182**, 496
- Emery, J. P., Burr, D. M., & Cruikshank, D. P. 2010, *AJ*, **141**, 25
- Gail, H.-P. 2004, *A&A*, **413**, 571
- Gartelle, G. M., Hardersen, P. S., Izawa, M. R., & Nowinski, M. C. 2021, *Icar*, **354**, 114043
- Gehrels, T. 1994, *Hazards due to Comets and Asteroids* (Tucson, AZ: Univ. Arizona Press)
- Gilmour, C. M., Herd, C. D., & Beck, P. 2019, *M&PS*, **54**, 1951
- Grady, J., & Tedesco, E. 1982, *Sci*, **216**, 1405
- Grimm, R. E., & McSween, H. Y., Jr. 1989, *Icar*, **82**, 244
- Hallenbeck, S. L., Nuth, J. A., & Daurantas, P. L. 1998, *Icar*, **131**, 198
- Hamilton, V. E. 2000, *JGR*, **105**, 9701
- Hamilton, V. E. 2010, *ChEG*, **70**, 7
- Hargrove, K. D., Kelley, M. S., Campins, H., Licandro, J., & Emery, J. 2012, *Icar*, **221**, 453
- Harris, A. W. 1998, *Icar*, **131**, 291
- Hasegawa, S., Marset, M., DeMeo, F. E., et al. 2021, *ApJL*, **916**, L6
- Henning, T. 2010, *ARA&A*, **48**, 21
- Herter, T., Adams, J., Gull, G., et al. 2018, *JAI*, **7**, 1840005
- Houck, J. R., Roellig, T. L., Van Cleve, J., et al. 2004, *ApJS*, **154**, 18
- Jäger, C., Dorschner, J., Mutschke, H., Posch, T., & Henning, T. 2003, *A&A*, **408**, 193
- Jäger, C., Mutschke, H., Begemann, B., Dorschner, J., & Henning, T. 1994, *A&A*, **292**, 641
- Jones, T. D., Lebofsky, L. A., Lewis, J. S., & Marley, M. S. 1990, *Icar*, **88**, 172

- Kelley, M. S., Woodward, C. E., Gehrz, R. D., Reach, W. T., & Harker, D. E. 2017, *Icar*, **284**, 344
- Kelley, M. S., 2021 sbpy, <https://github.com/mkelley/mskpy>
- Koike, C., Chihara, H., Tsuchiyama, A., et al. 2003, *A&A*, **399**, 1101
- Koike, C., Shibai, H., & Tsuchiyama, A. 1993, *MNRAS*, **264**, 654
- Lane, M. D., Glotch, T. D., Dyar, M. D., et al. 2011, *JGRE*, **116**, E08010
- Levison, H. F., Bottke, W. F., Gounelle, M., et al. 2009, *Natur*, **460**, 364
- Levison, H. F., Olkin, C. B., Noll, K. S., et al. 2021, *PSJ*, **2**, 171
- Licandro, J., Campins, H., Kelley, M., et al. 2011, *A&A*, **525**, A34
- Lisse, C., VanCleve, J., Adams, A., et al. 2006, *Sci*, **313**, 635
- Lowry, V. C., Hanna, K. L. D., Ito, G., et al. 2022, *PSJ*, **3**, 181
- Mainzer, A., Bauer, J., Cutri, R., et al. 2019, NEOWISE Diameters and Albedos V2.0, NASA Planetary Data System doi: [10.26033/18s3-2z54](https://doi.org/10.26033/18s3-2z54)
- Mainzer, A., Grav, T., Masiero, J., et al. 2011, *ApJ*, **736**, 100
- Marchis, F., Enriquez, J., Emery, J., et al. 2012, *Icar*, **221**, 1130
- Martin, A., Emery, J., & Loeffler, M. 2022, *Icar*, **378**, 114921
- Martin, A., Emery, J., & Loeffler, M. 2023, *Icar*, **397**, 115507
- Martin, A. C. 2022, PhD thesis, Northern Arizona Univ., <https://www.proquest.com/openview/4f6664f58e089ac4cd9abd591e59fb08/1>
- Martin, A. C., & Emery, J. P. 2023, *PSJ*, **4**, 153
- McAdam, M., Sunshine, J., Howard, K., & McCoy, T. 2015, *Icar*, **245**, 320
- McCord, T. B., & Sotin, C. 2005, *JGRE*, **110**, E05009
- Mommert, M., Hora, J. L., Harris, A. W., et al. 2014, *ApJ*, **781**, 25
- Morbidelli, A., Levison, H. F., Tsiganis, K., & Gomes, R. 2005, *Natur*, **435**, 462
- Morlok, A., Lisse, C., Mason, A., Bullock, E. S., & Grady, M. 2014, *Icar*, **231**, 338
- Mueller, M., Marchis, F., Emery, J. P., et al. 2010, *Icar*, **205**, 505
- Neese, C. 2017, ASTEROID TAXONOMY V1.0, NASA Planetary Data System doi: [10.26033/e1p3-xm59](https://doi.org/10.26033/e1p3-xm59)
- Nesvorný, D., Vokrouhlický, D., & Morbidelli, A. 2013, *ApJ*, **768**, 45
- Pirani, S., Johansen, A., Bitsch, B., Mustill, A. J., & Turrini, D. 2019, *A&A*, **623**, A169
- Salisbury, J. W., D'Aria, D. M., & Jarosewich, E. 1991, *Icar*, **92**, 280
- Sharkey, B. N., Reddy, V., Sanchez, J. A., Izawa, M. R., & Emery, J. P. 2019, *AJ*, **158**, 204
- Sheppard, S. S. 2010, *AJ*, **139**, 1394
- SOFIA/USRA, 2022a FORCAST Basic Photometry, https://github.com/SOFIAObservatory/Recipes/blob/master/FORCAST-Basic_Photometry.ipynb
- SOFIA/USRA, 2022b FORCAST Grism Spectra: Basic Inspection and Assessment, https://github.com/SOFIAObservatory/Recipes/blob/master/FORCAST-Grism_Inspection.ipynb
- Spitzer Science User Support and Instrument Teams and IRSA Science User Support Team 2017, Spitzer Data Analysis Cookbook, Version 6.0, <https://irsa.ipac.caltech.edu/data/SPITZER/docs/dataanalysis/tools/cookbook/home/>
- Sultana, R., Poch, O., Beck, P., et al. 2023, *Icar*, **395**, 115492
- Tedesco, E., Noah, P., Noah, M., & Price, S. 2004, IRAS Minor Planet Survey. IRAS-A-FPA-3-RDR-IMPS-V6.0. NASA Planetary Data System
- Tholen, D. J. 1984, Asteroid Taxonomy from Cluster Analysis of Photometry (Tucson, AZ: Univ. Arizona Press)
- Tholen, D. J., & Barucci, M. A. 1989, Asteroids II (Tucson, AZ: Univ. Arizona Press), 298
- Vernazza, P., Fulvio, D., Brunetto, R., et al. 2013, *Icar*, **225**, 517
- Vilas, F., & Smith, B. A. 1985, *Icar*, **64**, 503
- Weissman, P. R., A'Hearn, M. F., McFadden, L., & Rickman, H. 2002, Asteroids III (Tucson, AZ: Univ. Arizona Press), 669
- Yang, B., Lucey, P., & Glotch, T. 2013, *Icar*, **223**, 359
- Zolensky, M., Nakamura, K., Gounelle, M., et al. 2002, *M&PS*, **37**, 737